LAMINAR FLAME SPEEDS OF NANO-ALUMINUM/METHANE HYBRID

MIXTURES

A Thesis

by

TRAVIS GLENN SIKES III

Submitted to the Office of Graduate and Professional Studies of
Texas A&M University
in partial fulfillment of the requirements for the degree of

MASTER OF SCIENCE

Chair of Committee,	Eric. L. Petersen
Co-Chair of Committee,	M. Sam Mannan
Committee Member,	David A. Staack
Head of Department,	Andreas A. Polycarpou

December 2014

Major Subject: Mechanical Engineering

ABSTRACT

An existing flame speed bomb, which uses optical techniques to measure laminar flame speed, was employed to study the fundamental phenomena of flame propagation through a uniformly dispersed aerosol. In a previous thesis by Andrew Vissotski, the groundwork was laid to begin studies of hybrid flames. Beginning from these preliminary findings, the facility was upgraded to disperse dust into the test chamber through a strong burst of gas. This aerosol was then allowed to settle for a minimum of 45 seconds to ensure that the conditions inside the test chamber were quiescent and that the dust was uniformly distributed. Extinction of laser light through the resulting aerosol was measured through the large optical access with a 632.8-nm, 5-mW HeNe laser so that the mass of suspended nano-particles could be determined as a function of time up until combustion has occurred.

The particles used in these experiments were aluminum nano-particles with a manufacturer-stated average fundamental particle size of 100 nm. To properly quantify the particle distribution inside of the vessel, a scanning mobility particle sizer was employed to characterize the aluminum, resulting in an average particle size of 446.1 nm. With a calibrated extinction measurement, experimental suspended mass of aluminum was measured up to 90 mg. A hybrid mixture of Al/CH_4 was chosen to serve as the combustion medium and to provide a well-characterized parent fuel to measure the contribution of nano-aluminum on combustion.

Two series of experiments were performed, both at stoichiometric conditions: one with the mixture in air and the second with the mixture in a 70/30 N_2/O_2 mix. The results herein show a maximum decrease in flame speed, 5-7% from the neat mixture, when nano-aluminum is introduced. In the 70/30 N_2/O_2 mixture, the addition of aluminum results in a maximum decrease of 5 cm/s from the neat flame speed of 80.5 cm/s and in the air mixture, a 2 cm/s maximum decrease from 35.3 cm/s. A preliminary spectroscopic analysis was performed but was inconclusive. It was also found that the addition of nanoparticles cause the flame to become unstable faster when compared to the neat mixture of CH_4/air.

ACKNOWLEDGMENTS

First and foremost, I would like to thank my advisor and co-chair, Dr. Eric Petersen. Without his guidance, support, and dedication none of this would have been possible. He took me in as a junior during the summer of 2011, helping to mold me into the scientist and engineer I am today with helpful suggestions and instilling a need to perform the best experiment possible by looking at the small details. I would like to thank my co-chair, Dr. Sam Mannan, and my committee member, Dr. David Staack. I would also like to thank Dr. Chad Mashuga for substituting for Dr. Mannan during my oral defense.

A special thanks goes to Mario Gomez-Hernandez and his advisor Dr. Renyi Zhang for the use of their differential mobility analyzer/condensation particle counter and their time in both performing the experiments, as well as providing advice on data analysis. These measurements were crucial in characterizing the aluminum in our system.

I would like to thank my colleagues, past and present, for teaching me the ropes, their advice, and their help throughout the years. I thank Andrew Vissotski for his work before me in laying the foundation on which this thesis is built.

I thank my family and friends for their support throughout my education; I know that it has not always been easy for them.

TABLE OF CONTENTS

LIST OF FIGURES

vii

LIST OF TABLES

1. INTRODUCTION

Dust explosions in process industries cause millions of dollars in damage to facilities and incalculable damage to personnel, making the understanding of the mechanisms behind dust explosions a top priority to prevent such disasters. The long-term objective in this study is to establish a method of measuring laminar flame speed of an aerosol mixture to a higher degree of accuracy than has been achieved in previous studies. Accomplishing this objective will provide a means to gain a better understanding of the mechanisms that drive dust combustion. It is suspected that in most literature sources the largest amount of experimental error comes from the injection method and the resulting lack of knowledge about the particle size distribution and concentration of particles in the mixture at the time of reaction. Additionally, research on heterogeneous mixtures in constant-volume bombs is mostly limited to pressure data with an optical access (if any) just large enough to verify ignition has occurred. Due to a lack of optical access, there is a corresponding lack of information about the level of turbulence at the time of ignition, as well as the homogeneity of the aerosol. This uncertainty is exacerbated by the common method of introducing the dust and igniting it in these experiments, which is to force it in with a blast of compressed air and to ignite it within seconds, at the most. Although such methods are useful for characterizing dust combustion behavior in a comparative way, these limitations lead to data that are facility dependent and perhaps ill-suited to studying the mechanisms behind dust combustion.

In these studies, the dust is introduced into a combustion vessel via a blast of compressed air and then almost immediately ignited, for example after 60 ms in Dahoe et al. [1] and 400 ms in Cashdollar [2]. Because the aerosol is ignited so quickly, it is unlikely that the atmosphere inside the combustion vessel is quiescent or that the dust is equally distributed. This common method has proven adequate if the objective is to compare dusts on a relative basis; however, understanding of the fundamental combustion mechanisms requires finer control over the experiment. In the present study, improvements were made on an existing gas-phase, spherical flame vessel to introduce dust into a controlled environment in a repeatable fashion to measure the flame speed using existing optical methods.

A summarization of foundational work this thesis is based on follows in Section 2. The theory and modeling of the aluminum particles as heat sinks is found in Section 3. Section 4 consists of a description of the experimental facility including: the method to inject dust, characterization of the nano-aluminum, extinction measurements, and aerosol flame speed system. The results and discussion of the extinction, flame speed, flame structure, and spectra are presented in Section 5. Finally, conclusions and future work is given in Section 6.

2. BACKGROUND

The experimental setup and foundational work of this thesis is based on the initial work done by Vissotski [3]. In this preliminary study performed at Texas A&M University, two experimental methods were investigated with the goal of introducing dust particles into a fuel/air mixture to study the effects of the particles. The first and more sophisticated method of introducing dust is based on previous work by Kalitan and Petersen [4]. Schematics of the experiment and procedure are given in Figure 1.
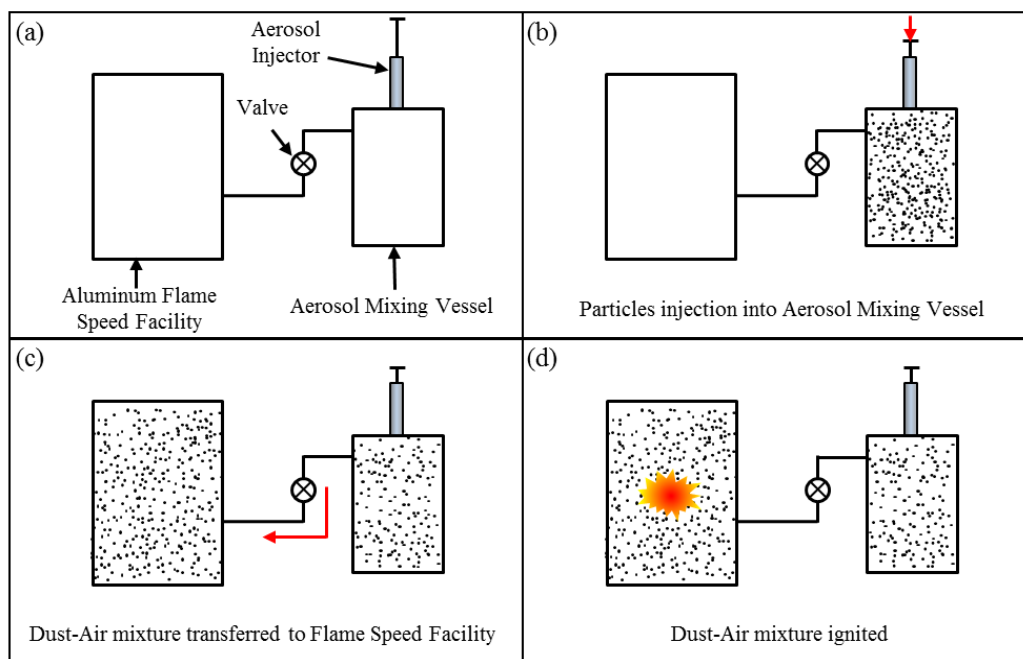
Figure 1. Experimental approach adapting previously developed particle injection technique by Kalitan and Petersen [4]. (a) Particles are loaded into the aerosol injector that is mounted directly to the Aerosol Mixing Vessel (AMV), (b) Particles are dispersed into the AMV, (c) The heterogeneous dust-air mixture is transferred to the Experimental Flame Speed Facility, and (d) Dust-air mixture is ignited at the center of the vessel with an electronic spark and flame propagation is recorded using the imaging technique. Taken directly from Vissotski [3].

Figure 1(a) shows the basic experimental setup, which includes a piston aerosol injector, aerosol mixing vessel, quarter turn valve, and the combustion vessel. The idea is to inject particles that are held at the front of the aerosol injection into the mixing vessel Figure 1(b). Here the particles are allowed to settle such that only the small particles remain. The resulting aerosol would be more uniform than the dust from which it was created. At a later time the valve would be opened, Figure 1(c), between the mixing vessel and the combustion vessel, which would be kept at a lower pressure. The suspended particles would then be transferred to the combustion vessel and at a set time would be ignited to perform the flame speed test, Figure 1(d). This approach had to be set aside because of issues with repeatability and because it was not scaled appropriately for the amount of suspended mass that these tests would require. It is possible that in the future this method will be revisited because it does have significant advantages with regard to uniform particle size and repeatability.

The next design was called the "direct-injection" method. Rather than use a separate vessel, it was decided to place the particles directly into the U-pipe that was inside the vessel. This modification would allow for greater mass loadings and subsequently greater suspended masses. Figure 2 is a schematic of how the "direct-injection' technique was implemented.
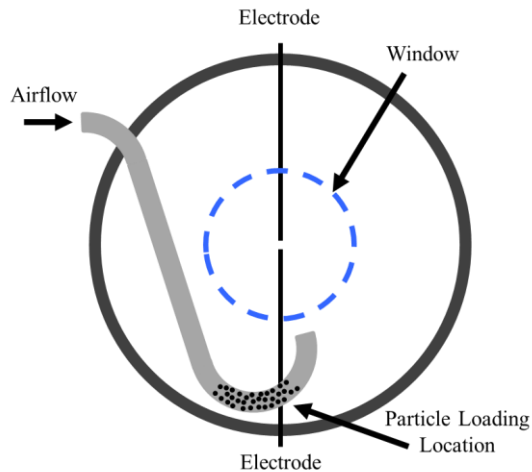
Figure 2. Schematic of "direct-injection" technique depicted in a radial cross-section of aluminum flame speed bomb. Taken directly from Vissotski [3].

The aluminum dust would be loaded into the U-pipe which was bent such that it would send the particles upward as they were injected. The U-pipe would not interfere with the line of sight of the schlieren optics as it would be below the window. Only a few tests were able to be performed with this setup. Figure 3 shows the suspended mass, measured with laser extinction, from two characterization tests.

Laser extinction works by measuring the attenuation of light being passed through a cloud of dust. Each particle will absorb or scatter a certain amount of light. An extinction efficiency factor, the sum of absorption and scattering efficiencies, is used to indicate how well a particle attenuates light, varying based on shape, size, and material. By knowing the extinction efficiency factor, number of particles (number density), and distance that the laser travels through the cloud of dust (path length), an estimation of suspended particle mass can be determined. A more detailed explanation is provided in Section 4.3.

5
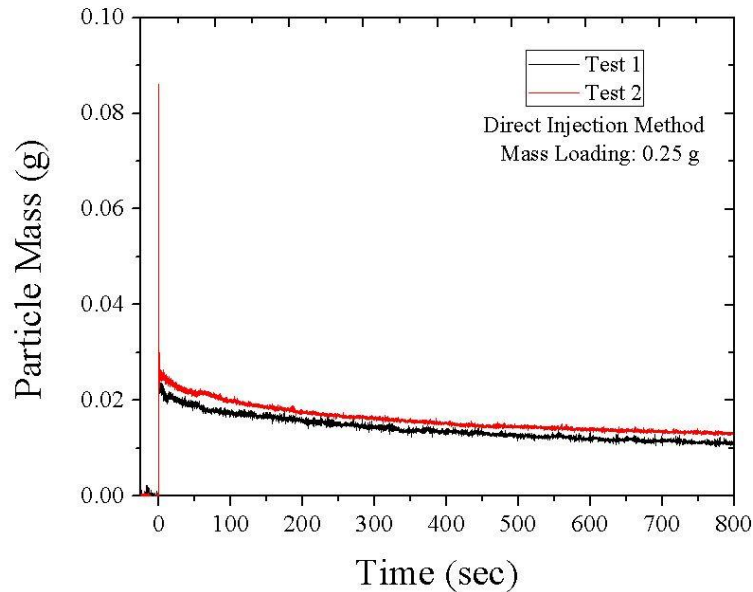
Figure 3. Instantaneous mass of nano-Al particles suspended within the aluminum flame speed vessel as a function of time. Calculated using particle number density and assuming 100-nm, solid aluminum spheres. Taken directly from Vissotski [3].

The method for obtaining the amount of suspended particle mass is very similar to the current experimental methods. However, the only difference between the previous study's method and the current study are the improvements, in the present work, made by better characterization of the aluminum and a qualitative error analysis. The repeatability between the two tests in Figure 3 was fairly good considering there were only two tests; however, an accurate representation of the true repeatability cannot be deduced from such a small sample size. By comparing the mass loading to the maximum particle mass, it is evident that the particle loss is high, 92%. The amount of suspended mass in Figure 3 is underestimated because of inaccurate constants used in calculation. If

the same signal were reanalyzed with updated constants the amount of suspended mass would likely increase. Figure 4 shows the results of the corresponding flame speeds.
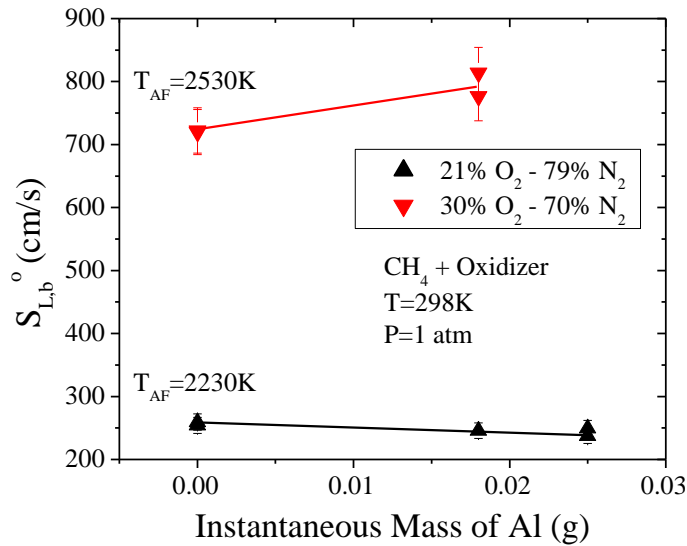
Figure 4. Burning velocity results for hybrid mixtures of Al nano-particles and stoichiometric Methane with different ratios of $O_2:N_2$ in the oxidizer. The lines are intended to serve as a visual aid. Taken directly from Vissotski [3].

The burned-unstretched flame speed appears to increase as the amount of suspended mass increases for parent mixtures, $CH_4/N_2/O_2$, at $\phi = 1$, an initial pressure of 1 atm, and that have adiabatic flame temperatures greater than the melting temperature of aluminum oxide. The parent mixtures for these experiments are stoichiometric mixes that vary the nitrogen dilution to change the adiabatic flame temperature. These results indicate that the flame speed should increase as aluminum is added for a nitrogen dilution of 30:70 $N_2:O_2$ and decrease for a dilution corresponding to air.

7

3. THEORY AND MODELING

There are three ways that the addition of aluminum could affect the flame speed kinetics: thermally, diffusively, and/or kinetically. To determine the contribution of diffusive and kinetic effects to the flame speed requires a well validated chemical kinetics mechanism, which unfortunately does not exist for aluminum at this time [5]. If the aluminum is assumed to be acting as a heat sink and diffusive/kinetic effects are kept constant, then it is possible to at least calculate how the adiabatic flame temperature drops as the energy from heat of combustion is absorbed by the aluminum. With a correlation between laminar flame speed and adiabatic flame temperature, the resulting change in flame speed can be found from this decreased adiabatic flame temperature. These calculations do not take into account aluminum combustion, and the thermal effect is only that of simple particle heating. Future calculations will include both contributions.

3.1 Heat Transfer

In order to simplify the later thermodynamic calculations, it would be convenient if the time scale for the aluminum to heat up would be very small compared to the experiment time. To get a better understanding of the time scale for a particle to heat up, a fundamental aluminum particle was evaluated as a transient heat transfer problem. It was assumed that the particle was a 100-nm sphere with a 4.5-nm aluminum oxide coating Figure 5. This assumption is based on the manufacturer's stated fundamental size, which was verified with SEM and TEM images in Section 4.2.
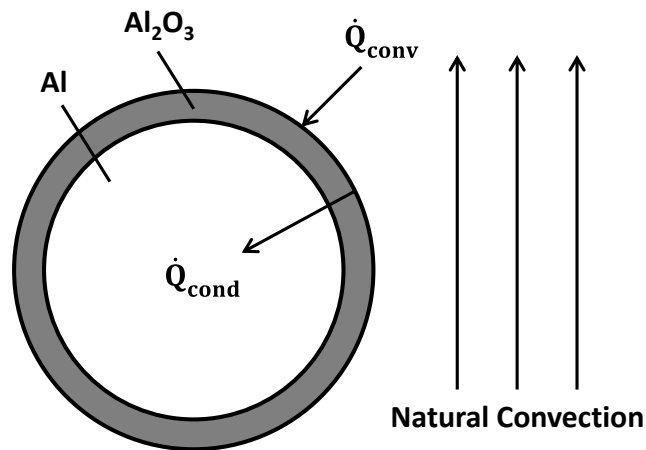
Figure 5. Schematic of heat conduction from hot gas products to nano-aluminum sphere.

Intuitively, it could be assumed that with such a small particle lumped capacitance would be a good approximation. To verify this assumption, the Biot number was calculated using Eqn. (3.1).

$$Bi = \frac{hR}{3k_{equiv}} \tag{3.1}$$

where h is the convective heat transfer coefficient, R is the particle radius and k_{equiv} is the equivalent thermal conductivity of the system based on the total thermal resistance of Al and Al_2O_3. The convective heat transfer coefficient was determined using Eq. (3.2), under the assumption that the system was in free convection [6].

$$\overline{Nu}_D = 2 + \frac{0.589Ra_D^{1/4}}{\left[1 + \left(\frac{0.469}{Pr}\right)^{9/16}\right]^{4/9}} \tag{3.2}$$

Eq. (3.2) becomes $\overline{Nu}_D = 2$ because the Rayleigh number, Ra_D, approaches zero. The reason for this is that there is a very small diameter term in the numerator which is cubed, dominating the equation. This results in the convective heat transfer coefficient being k_{air}/R. The resulting h is $4440000 \frac{W}{m^2 K}$. This makes the Biot number, Eq. (3.1), equal to 0.001, thus confirming that the assumption of lumped capacitance is reasonable ($Bi < 0.1$).

Several assumptions were necessary to calculate the time for the particle to heat up: lumped capacitance, negligible radiation, no contact resistance, negligible phase change time, and constant properties. It has been shown in the past that nano-particles can increase the convective heat transfer coefficient in fluids; however, since there was a small concentration this was also neglected [7, 8]. It was assumed that the particle started off at 298 K and the fluid temperature was 2500 K, approximately the adiabatic

flame temperature. The remaining material constants to solve Eq. (3.3) were taken at 300 K from Incropera [6].

$$t(T_f) = \frac{(\rho V c_p)_{Al} + (\rho V c_p)_{Al_2O_3}}{h4\pi R^2} \ln\left(\frac{T_i - T_\infty}{T_f - T_\infty}\right) \tag{3.3}$$

The resulting time it takes the sphere to heat up to 99.9% of the adiabatic flame temperature was approximately 90 ns. This small time scale is supported by Hu [9], where the time to dissipate heat is on the order of picoseconds using 50-nm spheres of gold, as well as by Petersen [10]. Because the particles heat up extremely fast, the rest of the thermodynamic calculations can be done neglecting time dependence.

3.2   Conservation of Energy

Time dependence can be neglected so the thermodynamics can be looked at as a simple balance of energy. On one side is the amount of energy required to heat and cause the particles to change phase and on the other is the change in energy between the adiabatic flame temperature and the final temperature. This energy balance is explicitly defined in Eq. (3.4).

$$\sum N_k \left(\bar{c}_V (T_f - T_i) + \Delta \bar{h}_{fus} \right)_k = N_{Prod} \bar{c}_{P,mix} (T_{ad} - T_f) \tag{3.4}$$

This equation is calculated entirely on a molar basis. The LHS is the sum of the chemicals that compose the particles, Al and Al_2O_3. The moles of Al and Al_2O_3 were found by knowing the fraction of the fundamental particle that is Al. It was then assumed that there is some amount of suspended particle mass which can then be broken down into Al and Al_2O_3. Throughout the thesis, suspended mass of aluminum is used;

11

this refers to the aluminum particles which contain both Al and Al_2O_3. Eq. (3.4) can be simplified into Eq. (3.5) knowing that the final temperature is likely to be in the range where both Al and Al_2O_3 are liquid and that the RHS will only contain the sensible enthalpy because the enthalpy of formation cancels between the two temperatures.

$$\sum N_k \left(\Delta \bar{h}_{T_f} - \frac{P_0}{\rho} + \Delta \bar{h}_{fus} \right)_k = \Delta H_{gas,T_{ad}} - \Delta H_{gas,T_f} \qquad (3.5)$$

Here P_0 was taken as 1 atm, enthalpies were evaluated using NIST equations or the AramcoMech 1.3 thermodynamic data, density, ρ, and latent heat of fusion shown in Table 1 [11-14]. The densities were calculated using correlations from Ikemiya [15] and Assael [16].

Table 1. Temperatures and latent heats for Al and Al_2O_3

	T [K]	Latent Heat [kJ/mol]
$Fusion_{Al}$	933.45	10.71
$Vaporization_{Al}$	2793	314
$Fusion_{Al_2O_3}$	2345	116.02
$Vaporization_{Al_2O_3}$	3250	

To solve the RHS of Eq. (3.5), the assumption is made that complete combustion occurs and the only species are H_2O, CO_2, and N_2. The number of moles of each is found by using the ideal gas law and the known dimensions of the vessel. The final temperature can be evaluated with the above information and methodology, but the final step from temperature to laminar flame speed remains.

The CHEMKIN PREMIX module was run for various mixtures of stoichiometric $CH_4/N_2/O_2$ wherein the nitrogen-to-oxygen content was varied. In varying the nitrogen dilution, the adiabatic flame temperature is modified with very little change to the diffusive and kinetic characteristics. The results of these simulations are shown with an exponential fit in Figure 6.
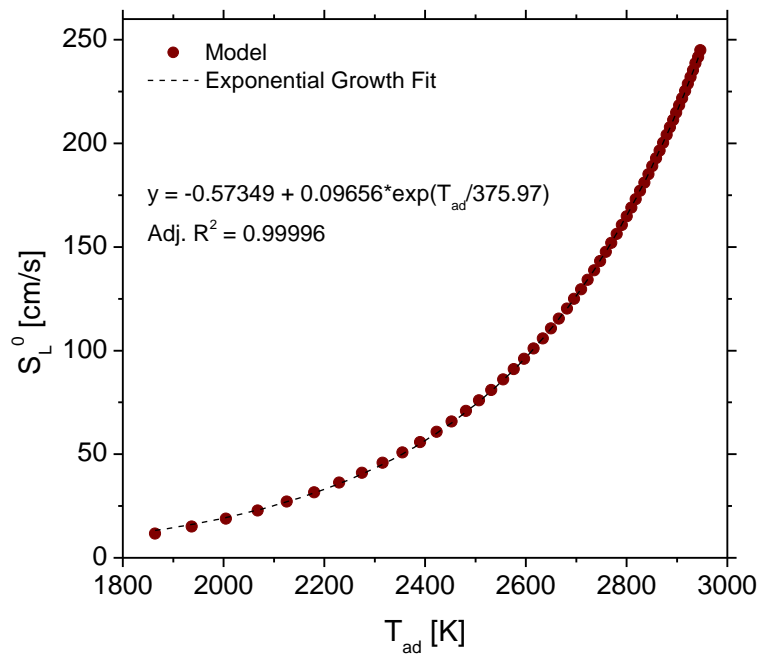
Figure 6. Model results of flame speed of $CH_4/O_2/N_2$ as a function of adiabatic flame temperature fit as an exponential growth for easier computation.

With the correlation shown in Figure 6, any flame speed of a $CH_4/N_2/O_2$ within the bounds of the tested mixtures can be found by knowing its adiabatic flame temperature. The resulting flame speed has very little error associated with it, as the exponential growth fit has a very high R^2 value, and subsequently a very low sum of

squared error. The final results of Eq. (3.5) for both a nitrogen dilution of 70:30 N_2:O_2 and air are given in Figure 7.
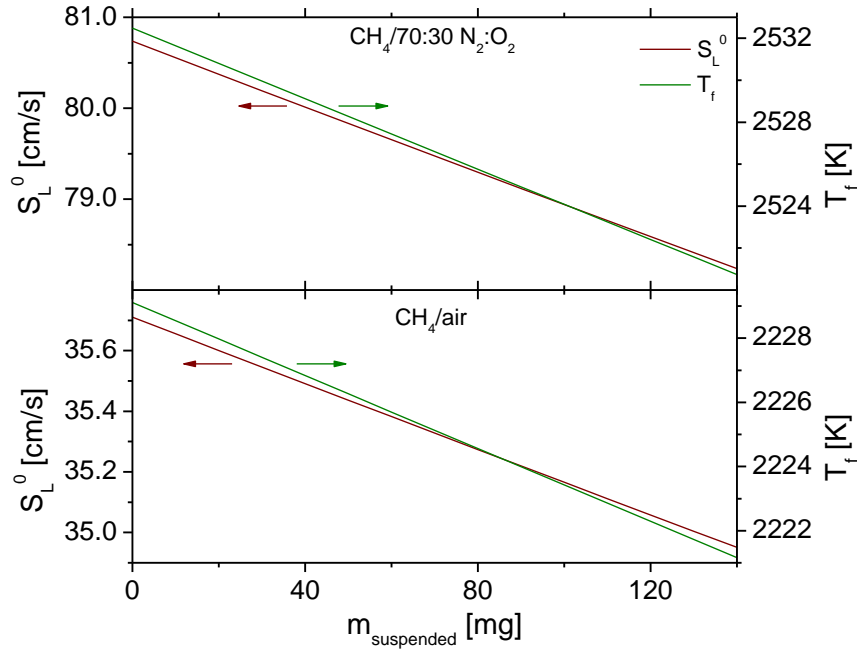
Figure 7. Laminar flame speed and the final adiabatic temperature with the aluminum acting as a heat sink in a (top) CH_4/70:30 N_2:O_2 mixture (bottom) CH_4/air mixture.

Both of these figures show a decrease in flame speed, though not a large reduction. In the case of the 70:30 N_2:O_2, it is a decrease of 2 cm/s with a suspended mass of aluminum of 140 mg; and for air it is less than 1 cm/s. Note as well that the corresponding decrease in flame temperature is only about 2 − 6 K over the range of aluminum mass loading of interest herein. Hence, if aluminum were acting solely as a heat sink, the flame speed should decrease at an almost linear rate, with respect to the suspended mass, by 1-2 cm/s.

4. EXPERIMENTAL FACILITY AND APPROACH

The low-pressure laminar flame facility at Texas A&M University is a 28.1-L, 35.6-cm long cylindrical vessel designed to be filled with gas-phase components up to a maximum initial pressure of 5 atm. The vessel is filled using the partial pressure method using two pressure transducers with precisions of 0.1 torr and 0.1 psi. Fuel-air mixtures are ignited using a central ignition system, and the resulting flame propagation is captured using a high-speed camera in a Z-type schlieren setup. For additional information regarding the existing flame speed facility, including equipment, testing procedure and theory, see the earlier works of de Vries [17] and Lowry et al. [18].

4.1   *Dust Injection*

This study is based on a variant of a "direct-injection" method [3]. The objective during the system design was to create a method of performing tests quickly, while still maintaining a highly repeatable experiment from test-to-test. One way of accomplishing the objective was to minimize the amount of piping that the dust would have to flow through to get to the experimental vessel. The first design iteration included a single quick-connect fitting placed right before the filling tube enters into the vessel. The schematic for this design is shown in Figure 8.
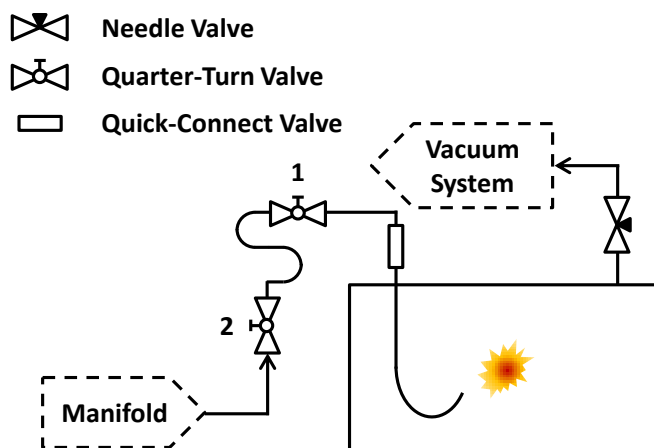
Figure 8. Schematic of initial piping for gas filling and aerosol dispersion.

The method of filling using this first version of the experiment was to slowly vacuum the vessel down to 745 torr using the needle valve and then close the vessel off to both vacuum and the manifold by closing the quarter turn valve 1 (Figure 8). The curved section was made to maximize the amount of volume that could be held because of a limited amount of space. This section was then pressurized to 172.5 psi and then subsequently closed off to the manifold through quarter turn valve 2. These pressure values were determined to create a 1-atm pressure inside of the vessel when quarter turn valve 1 was opened. This pressure difference pushes the dust out of the piping system and into the vessel through a curved pipe, shown inside the vessel (Figure 8). The curved pipe directs the particles up and slightly towards the center of the vessel so that they could then settle and disperse uniformly.

A short series of tests was needed to determine what combination of pressures to use in the pressurized section and the initial vessel pressure to result in 1-atm pressure

after the injection process. It was decided to first test what the pressure would equalize to if the section after valve 2 was at atmosphere and before it was vacuumed. This consideration was only necessary because a static pressure gauge was not installed inside the vessel at the time of these experiments. The pressures were then varied over a region that would allow for a multiple regression to be performed. The results of these characterization tests can be seen in Table 2.

Table 2. Pressure equilibrium experimental results

$P_{Initial}$ [torr]	$P_{Pressurized}$ [psi]	P_{Final} [torr]
730	50	700
740	50	709.6
740	100	714
740	150	718.6
750	50	718.9
750	100	723.6
760	14.7	725.3
760	14.7	725.4
760	14.7	725.4

The multiple regression resulted in a line for when the final pressure equilibrated to 1 atm. This fit is shown in Figure 9. It was decided to stay below 200 psi to remain well within the margin of safety for the tubing and fitting. It was also necessary to have a sufficiently high pressure in the pressurized section to push as much dust out as possible.

The compromise between these two needs is the previously mentioned 745 torr initial pressure and 172.5 psi pressurized value.
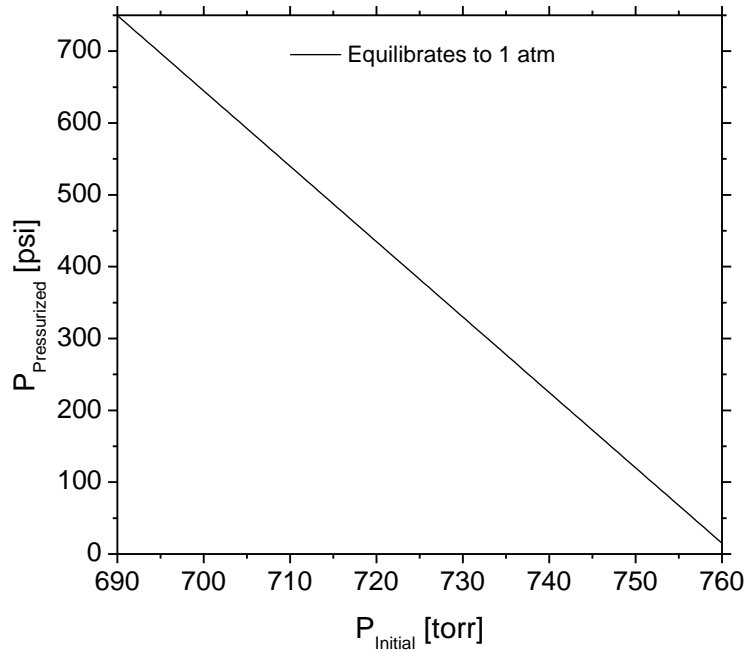
Figure 9. Initial and pressurized section to equilibrate to 1 atm after injection**.**

The first design iteration was ultimately rejected because of a lack of repeatability and safety concerns. Ultimately, the only way to add dust to the vessel was to scoop it into the pipe; however, to maintain repeatability the dust has to be weighed beforehand. This weight is what is referred to herein as the mass loading. Because of this required step, it is suspected that dust was being lost during the transfer process. The safety concern here was the dust that was potentially lost during the transfer process. In addition to the safety concern, there was also a problem because the extinction tests

performed at that time (see below for details) had a large amount of scatter in the results, thus it was determined that a new method of introducing the dust was needed.

From the experiments performed previously, the theory is that the loss of mass during transfer of the powder was the main source of non-repeatability. To minimize the mass loss, a new setup was employed wherein a section of pipe was removed, a U-pipe, so that the mass loading is now measured inside the U-pipe rather than being transferred to it. A schematic for the current design is shown in Figure 10.
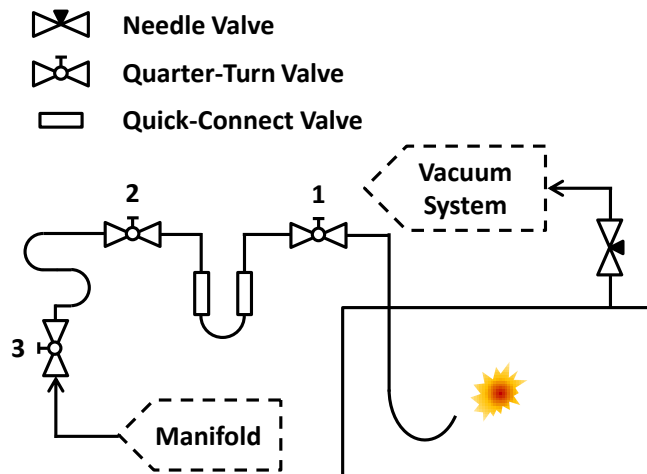
Figure 10. Final schematic of piping for gas filling and aerosol dispersion.

The method of introducing the dust using this version is similar to that of the previous one. First, the entire system is evacuated and filled to the laboratory atmospheric pressure with the required gas mixture. Then, quarter turn valve 1 (Figure 10) and the needle valve are closed off and the gas mixture is vacuumed out of the manifold and up to valve 1 using the manifold vacuum. Atmospheric air is then

introduced through the manifold until the pressure is again atmospheric pressure, at which point quarter turn valve 2 (Figure 10) is closed off. The u-pipe is disconnected from both quick connect valves, and dust is scooped into it until it reaches the required mass loading. The u-pipe is placed back into the system, and the manifold is again vacuumed out and filled with the gas mixture. These steps ensure that the gas mixture does not come into contact with the laboratory atmospheric air at any time. All valves are then opened, and the entire system is very slowly vacuumed out to 745 torr using the needle valve. After reaching the set pressure of 745 torr, the system is closed off at valve 2. Once again the section between valves 2 and 3 is pressurized using nitrogen or air to 172.5 psi. To initiate the experiment, valve 2 is opened rapidly, allowing the higher-pressure gas to pass through and induct the particles into the chamber. After each experiment, the vessel is flushed 10 times by filling the entire line up to valve 1 to roughly 190 psi and quickly opening the valve while the vessel is under a slight vacuum. The manifold is opened to atmosphere when the system is below one atmosphere to provide a steady flow to entrain dust particles out of the vessel. This is done 10 times for 10 minutes each. This design achieved the objective of being easy to load particles for a new experiment and has been shown to be suitably repeatable using extinction tests which are described below.

4.2   Nano-Aluminum Characterization

It is assumed that each individual particle is a perfect sphere of diameter 100 nm because the chosen dust is a 100-nm nano-aluminum purchased from US Research Nanomaterials, Inc. This dust was used because of the nature of the testing procedure, which can occur over several minutes. The particles must be very small so that they stay suspended long enough for the air to become quiescent, and so that the particles' surface area is maximized to promote a quick reaction. To verify that the fundamental particle size of the nano-aluminum is close to the manufacture's claim, the material has been analyzed using both SEM and TEM in Figure 11. To isolate the agglomerate in (b) of Figure 11, the nano-aluminum was first suspended in nitromethane and sonicated to break up any large agglomerates. This mixture was then put into a carbon mesh and the nitromethane evaporated off. The mesh containing the nano-aluminum was then placed into the TEM for imaging.
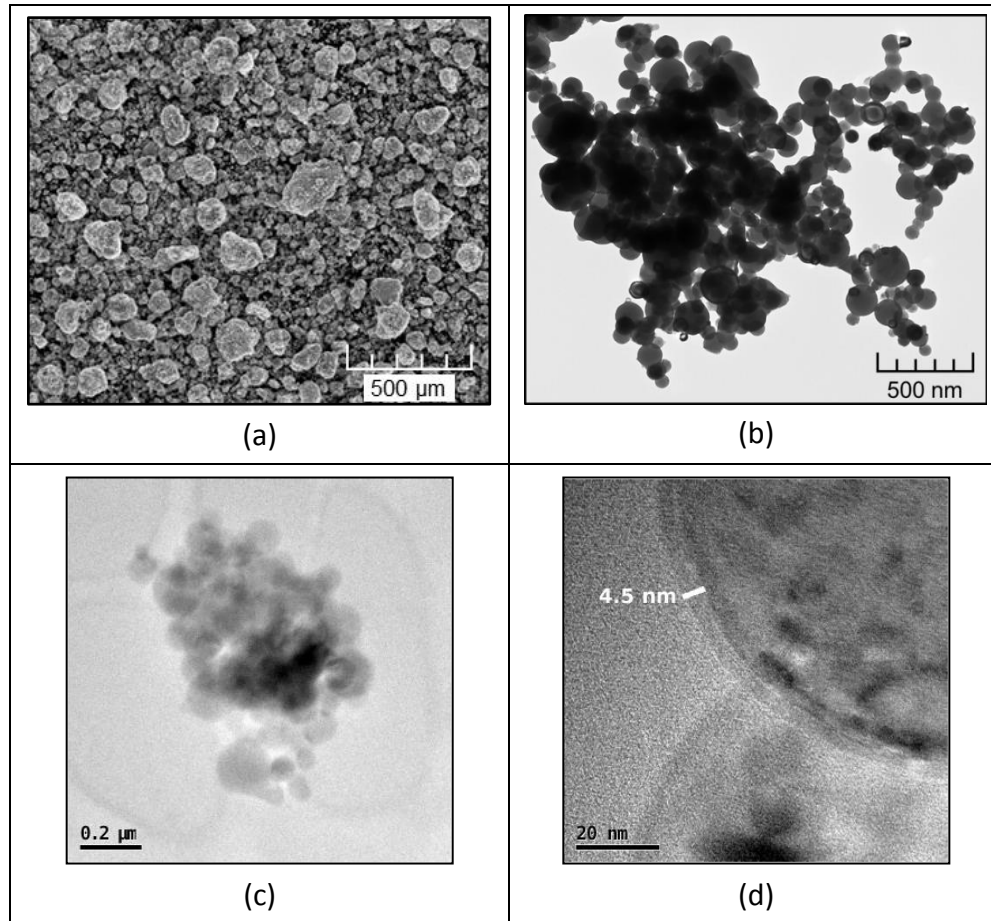
Figure 11. (a) SEM image of 100-nm nano-aluminum raw dust purchased from US Research Nanomaterials, Inc. showing 100-µm agglomerates, (b) A close up TEM image showing fundamental particle sizes after being processed, (c) Another TEM image of an aluminum agglomerate [19], and (d) Zoomed in from (c) showing an individual nano-particle's Al_2O_3 shell [19].

Based on these images, the fundamental particle size is close to the manufacture's claim, and it can be assumed that there is roughly a 50-nm standard deviation. The TEM image gives an indication of the aluminum oxide layer which is approximately 4.5 ± 0.5 nm. Knowing the size of this layer, the approximate size of the fundamental particle, and known densities of aluminum and alumina, the average density

can be calculated to be 3.01 ± 0.14 g/cm^3. The reason that the fundamental particle size is used, instead of the average agglomerate size, is because of the assumption that all particles are perfectly spherical; therefore, if a larger particle diameter were assumed it would inherently lower the calculated percentage of the particle that is Al_2O_3. This would be unrealistic since the agglomerates are composed of individual particles. The size of the agglomerates does become an issue however when trying to estimate the amount of suspended mass in the vessel; the method used to measure the amount of suspended mass is discussed later in Section 4.3.

A distribution curve is needed to establish what size agglomerates are actually being injected and subsequently suspended in a typical experiment of interest herein. To determine the distribution curve of the actual agglomerates in a real experiment, a combination of a differential mobility analyzer (DMA) and condensation particle counter (CPC) were used to pull particles from the vessel and analyze them. A simplified schematic of the setup is shown in Figure 12.
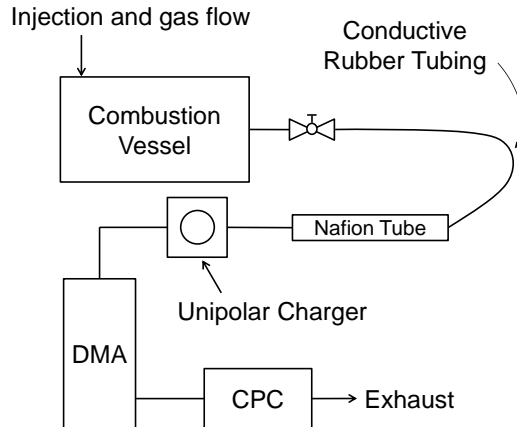
Figure 12. Schematic of the DMA/CPC used to determine the particle loading in the vessel.

An aerosol is created inside of the combustion vessel using the standard injection process described in the previous section and shown schematically in Figure 10. At this time, a quarter-turn valve is opened and the aerosol is pulled from the vessel and through the conductive rubber tubing, chosen to prevent particles sticking to the walls, by a 1.5-SLPM vacuum pump located before the exhaust. The aerosol is dehumidified with a Nafion tube and then pulled through a unipolar charger to polarize the particles for the DMA. At this point, the aerosol is conditioned for the data-taking part of the experiment in which the DMA ramps voltage up and down to determine particle size and the CPC counts them. Finally, the remaining gas is exhausted to the test cell exhaust system. After each experiment, the system was purged to prevent contamination. The DMA/CPC setup could not see pressures much below 1 atm, and so the combustion vessel had to be open to atmosphere. To prevent contamination from particles in the air, a filter was placed at the opening to atmosphere. The data retrieved from this experiment are

continuous and integrated over 15-30 second intervals. These intervals corresponded to the time it takes the DMA to change either to or from maximum to minimum voltage. The raw data of a representative experiment, as well as the portion of raw data used in determining the average particle distribution, are shown in Figure 13.
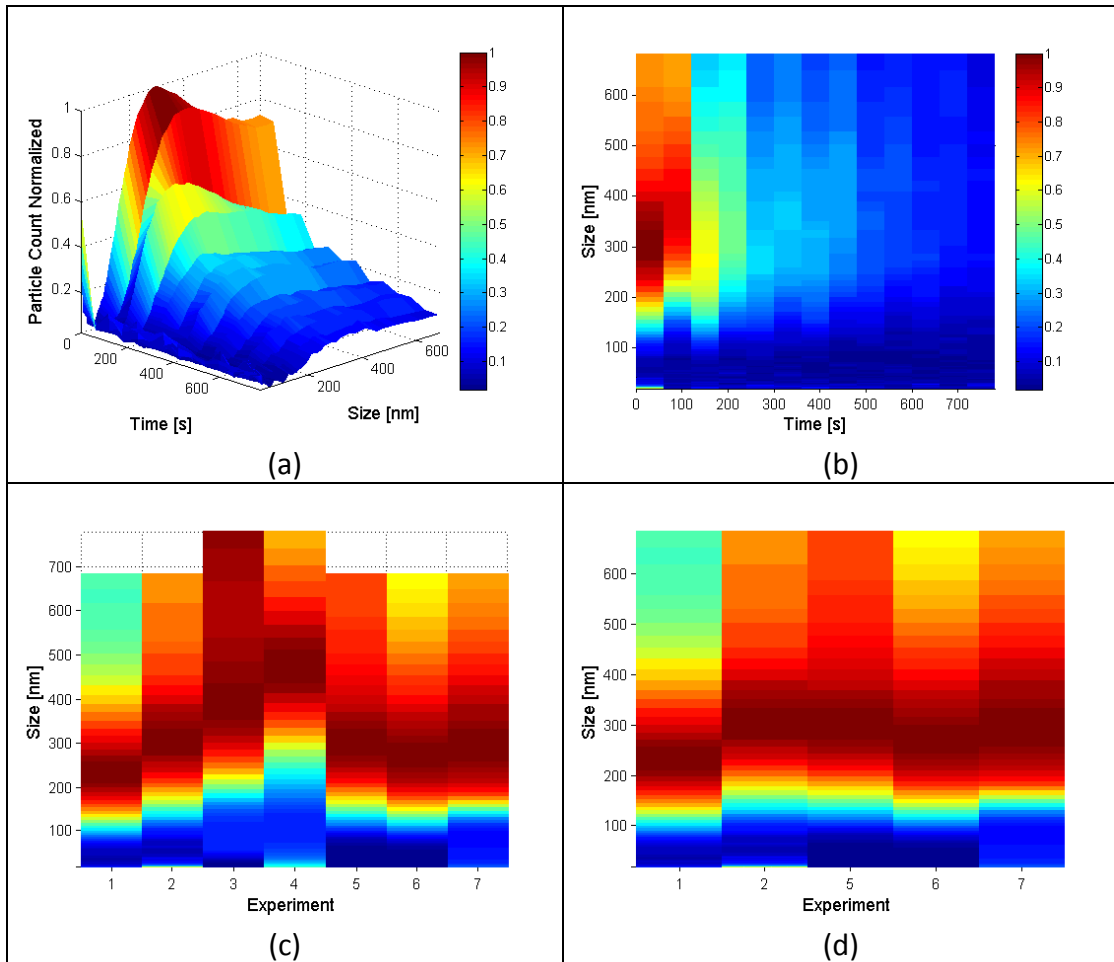
Figure 13. Experimental data from DMA/CPC (a) Representative data from one experiment; (b) The same data as (a) plotted looking down the z-axis with color denoting the particle count normalized; (c) Each experiment's distribution at the time containing the highest average maximum particle count; and (d) Same data as (c) with experiments deviating significantly from the group removed.

The graphs in (a) and (b) of Figure 13 show the same data. In graph (a), the particles have been normalized by the maximum of the experiment, and this is plotted against time and size. As expected, the number of particles decreases with time because the particles are slowly falling down due to natural settling of the larger agglomerates. More importantly, the injection process is not a continuous process as it is done in a single burst; therefore, as the particles are being pulled out to sample, the concentration inside of the vessel is decreasing. This unavoidable particle depletion limits the amount of data that can be used for analyzing the size distribution to a single time step with the highest number of sample points. The maximum peak is not necessary at the same time for all experiments because the particles travel through the piping, from the vessel, to the DMA/CPC for some duration. Graph (c) shows the time period with the highest number of sample points for each of the seven experiments. Two of these tests were immediately thrown out because they did not match the rest of the experiments, and the remaining experiments are shown in (d). It was of interest to measure if particle contamination would matter between experiments so minimal flushing was performed during these two rejected tests. When the results differed significantly, it was concluded that flushing does matter and the effected experiments were disregarded. The results of experiment seven were also thrown out because they did not follow a lognormal distribution like the others, and it was concluded that there must have been problems with the experiment, such as insufficient flushing.

The DMA is limited in the maximum size it can detect because at large sizes a very high voltage is required, increasing the probability of error in the equipment. At the

lower end, it was noted that in several experiments there is an unusually high number of particles; this is possibly due to the filter not removing all of the particulates in the air or contamination of small particles from previous tests. For these reasons, the lognormal fits, a typical distribution used to describe aerosols, for the remaining four experiments were calculated by removing outliers at either end of the distribution, Figure 14.
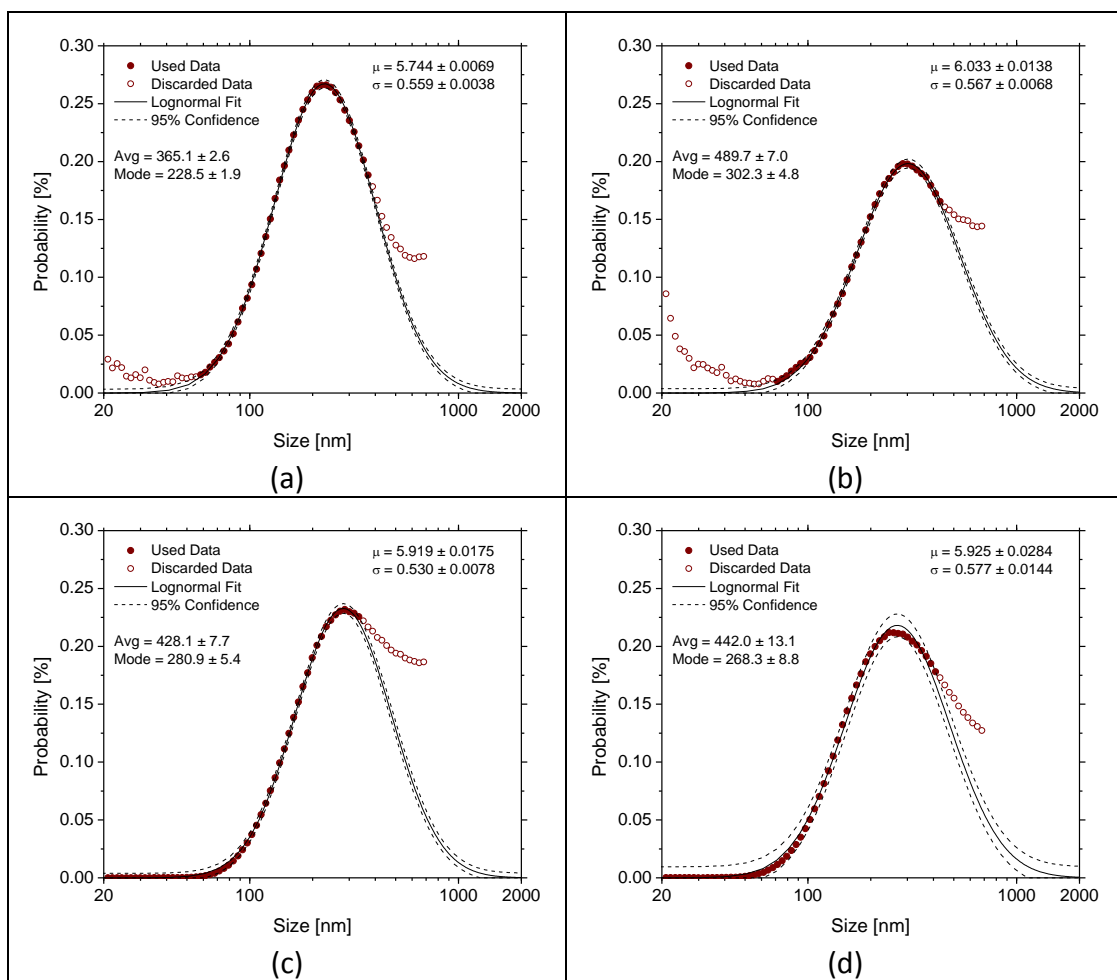
Figure 14. All plots are on a semi-log graph. (a) Experiment 1 distribution and lognormal fit; (b) Experiment 2 distribution and lognormal fit; (c) Experiment 5 distribution and lognormal fit; and (d) Experiment 6 distribution and lognormal fit.

In all of these graphs, the y-axis is probability, whereas in previous plots the distribution is a function of the number of particles normalized. The transformation between the two is done by fitting each of the curves to a lognormal curve that is scaled by some factor, a. The equation for this probability density function is given in Eq. (4.1).

$$Pr = \frac{a}{x\sqrt{2\pi\sigma}} \cdot \exp\left(-\frac{(\ln x - \mu)^2}{2\sigma^2}\right) \tag{4.1}$$

where Pr is the probability, x is size and (σ, μ) the scale parameter and location parameter that are fit. The experimental data points are scaled by the inverse of the fit scaling factor, a. Initially all data points were divided by some combined scaling factor but that washes out the differences in distribution between experiments. In comparing the four plots in Figure 14 to each other, it becomes apparent that the distribution of experiment 1, (a), is very different from the other three experiments. Given that this Experiment 1 was the first experiment performed, where improvements and procedures were still being revised, it was decided to remove this experiment from the final distribution leaving only experiments 2, 5 and 6. Combining the three experiments and fitting a lognormal distribution to them is done in Figure 15.
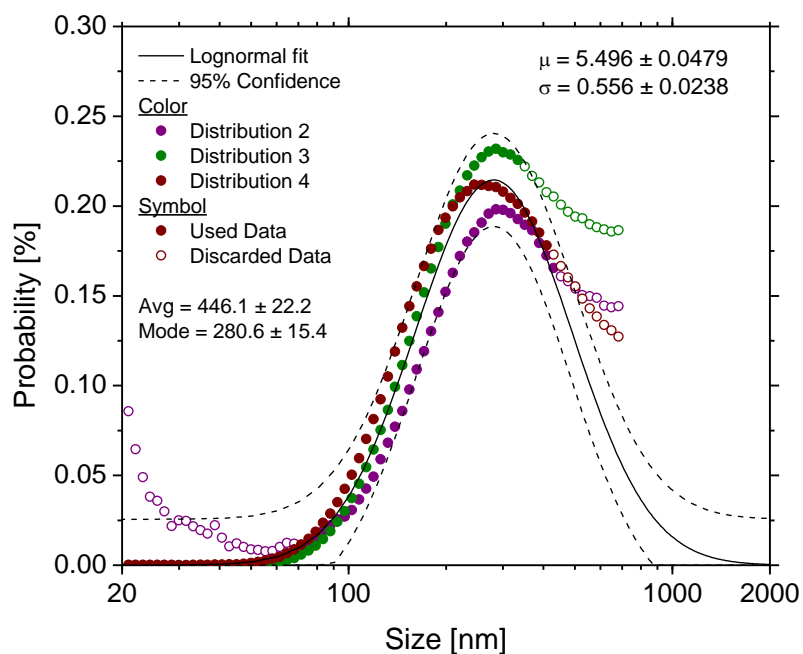
Figure 15. Aluminum distribution curves on a semi-log plot. Experimental data used in finding the lognormal fit shown as solid points, open points show excluded data, a lognormal fit is shown as a solid line, and the 95% confidence interval is shown in dashed lines.

Figure 15 shows the experiments used for calculating the size distribution with the resulting fit. The experiments collapse very well at lower sizes and start to deviate from one another slightly at 100 nm. Nonetheless, it is seen from this plot that the confidence interval properly captures the variance between the different experiments. The only points that are outside of the 95% confidence interval are the points that have already been discarded. A more-simplified plot is shown Figure 16.
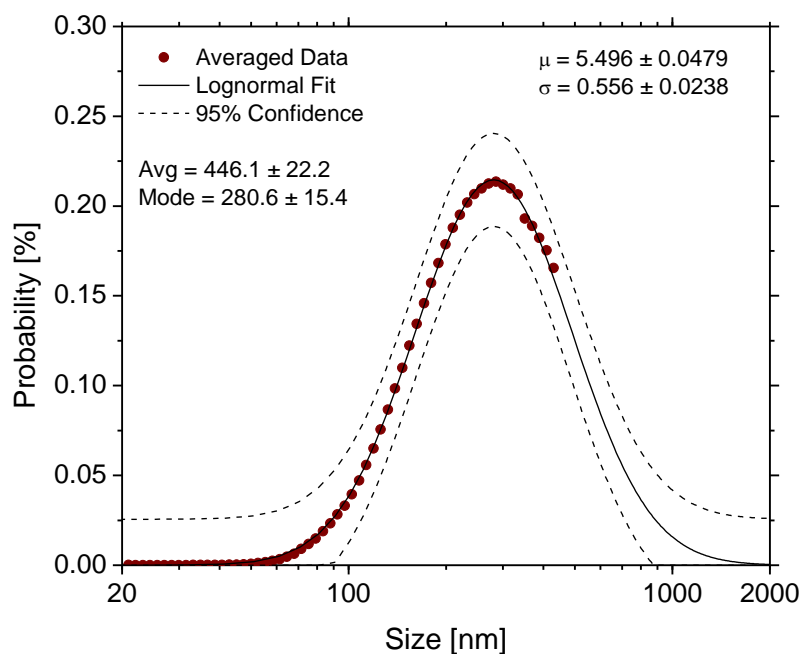
Figure 16. An aluminum distribution curve on a semi-log plot. Averaged experimental data shown as points, a lognormal fit is shown as a solid line, and the 95% confidence interval is shown in dashed lines.

The data points in Figure 16 are the averaged experimental values. The point of discontinuity occurs because, from the point onward, only one experiment still has data that have not been discarded from the individual fits. The most probable size is 280.6 ± 15.4 nm, so if any agglomerates could be isolated after injection, it is most likely this size would be found. The laser extinction method discussed in the next section requires an average agglomerate size, which was found to be 446.1 ± 22.2 nm.

4.3   Extinction

It is vital to be able to measure the amount of mass as a function of time in these

experiments for both repeatability and, most importantly, to know the amount of

suspended mass at the time of combustion. The method chosen was a non-intrusive laser

extinction technique based on the Beer-Lambert Law, which relates the attenuation of

light to the extinction from particles [20]. The laser setup created to measure the light

attenuation from the suspended dust in the combustion vessel is shown in Figure 17.
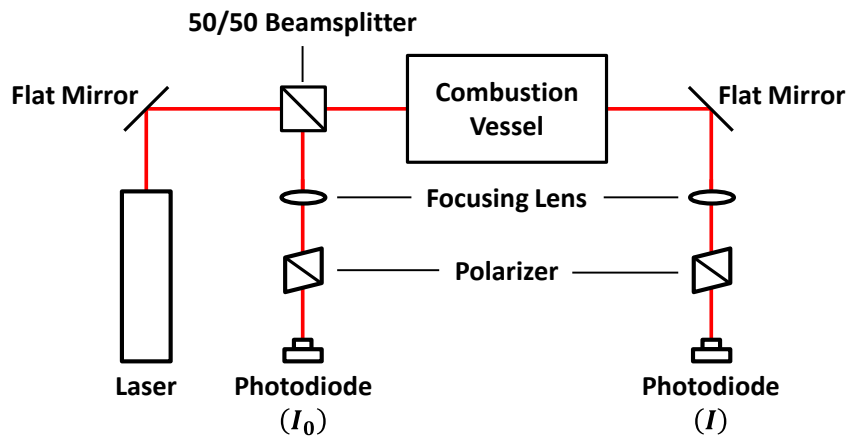
Figure 17. Schematic of extinction diagnostic laser setup. The laser light
is at 632.8 nm from a HeNe laser.

In this setup, the laser beam is sent through a 50/50 beamsplitter, which splits the

laser light and sends roughly half of it to the first photodiode and the rest through the

combustion vessel and ultimately onto a second photodiode. The signal from the first

photodiode is denoted by I_0 and that of the second photodiode by I. The focusing lenses

are needed to focus the laser into the photodiodes for maximum signal. The polarizers are used to set I_0 and I equal to each other before any dust is introduced.

As mentioned before, these two signals are then combined and used to evaluate the mass of particles in the chamber based on the Beer-Lambert Law shown in Eq. (4.2) [20].

$$\frac{I}{I_0} = \exp(-N C_{ext} L) \tag{4.2}$$

where N is the particle number density, $\# \, particles/volume$, L is the path length or the distance that contains particles, and C_{ext} is the extinction cross section. Since the wanted, unknown variable here is N, another equation for C_{ext} is used, Eq. (4.3). For more information on this derivation, see Bohren and Huffman [21].

$$C_{ext} = Q_{ext} \frac{\pi}{4} d^2 \tag{4.3}$$

Here, d is the particle diameter, which is assumed to be the average particle diameter, and Q_{ext} is the extinction efficiency factor. The extinction efficiency factor is a measurement of how well a given particle attenuates light. So, the higher the extinction efficiency factor, the fewer particles are required to block light and decrease its intensity. Now the only unknowns are N and Q_{ext}. If Q_{ext} were known, then the suspended mass could be found using Eq. (4.4).

$$m_{susp} = N V_V (\rho V)_{Particle} \tag{4.4}$$

In Eq. (4.4), V_v is the vessel volume, $\rho_{particle}$ is the average density of the suspended particles, and $V_{particle}$ is the average volume per suspended particle. For a

cylindrical vessel and assuming all particles are spheres, Eqs. (4.2)-(4.4) can be simplified to Eq. (4.5).

$$m_{susp} = \frac{-\pi (d\rho)_{Particle} d_V^2}{Q_{ext}} \ln\left(\frac{I}{I_0}\right) \tag{4.5}$$

A similar equation can be derived for the mass concentration, γ_{susp}, shown in Eq. (4.6).

$$\gamma_{susp} = \frac{-4(d\rho)_{Particle}}{l_{Vessel} Q_{ext}} \ln\left(\frac{I}{I_0}\right) \tag{4.6}$$

where l_{Vessel} is the interior length of the combustion vessel. For both Eq. (4.5) and Eq. (4.6), the only missing information for any given experiment is Q_{ext}.

Since there is already an assumption that the particles are perfect spheres, this scenario becomes a classic case of Mie scattering, which is one solution to the Maxwell's equations, to analytically solve for Q_{ext}. There are many different methods and programs available to calculate scattering by spheres. The program chosen is called MieLab [22]. It is a fairly recent program, but aluminum is not available to select as a material so it had to be manually input. The values required are the light frequency, bulk damping constant, Fermi velocity, atomic density, and material refractive index. The values for light frequency, bulk damping constant, and Fermi velocity were found in D.R. Huffman [23]. The material refractive indices were found in A.D. Rakić [24]. With MieLab prepared to use aluminum, Figure 18 was created.
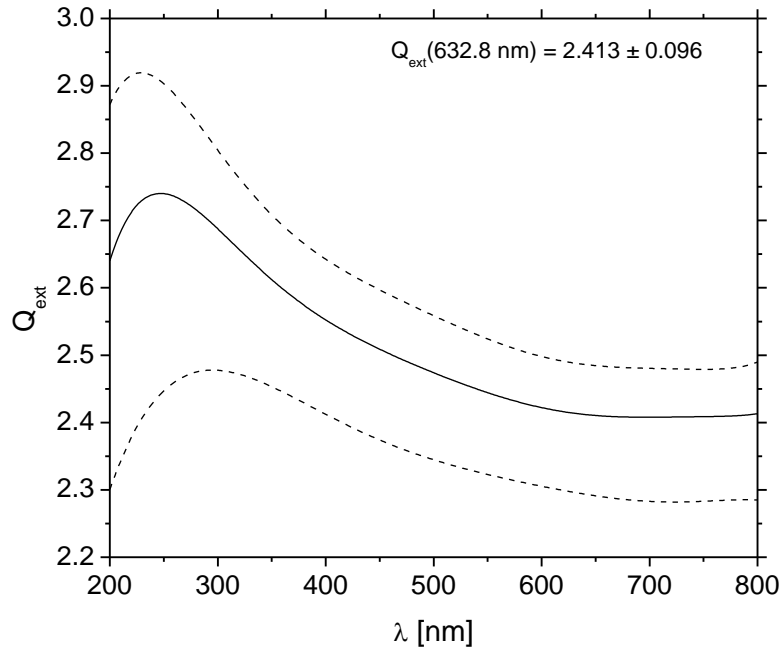
Figure 18. Theoretical efficiency factors as a function of wavelength from MieLab given the distribution shown in Figure 16.

Since this experiment uses a 632.8-nm, 5-mW Helium-Neon (HeNe) laser, the corresponding extinction efficiency factor, Q_{ext}, is 2.413 ± 0.096. With Q_{ext} approximated as such, Eq. (4.5) can be used to estimate the amount of suspended mass of aluminum at any given point in time, integrated along the laser beam path length. Likewise, Eq. (4.6) can be used to calculate the suspended concentration of aluminum.

With all variables known, suspended mass can now be calculated from signal data. Employing Eq. (4.5) or Eq. (4.6) requires some additional processing of experimental data. An example of what raw signal data can look like is shown in Figure 19.
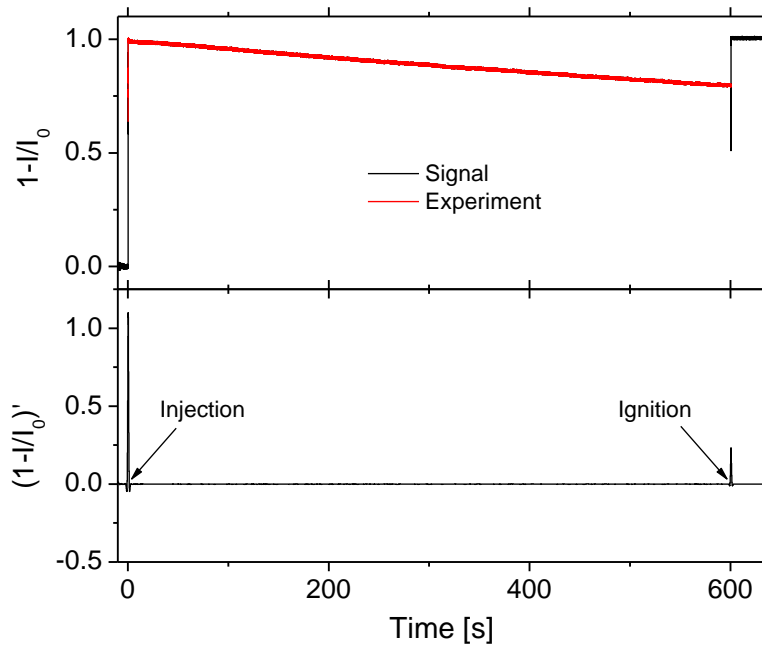
Figure 19. Raw signal data and their derivative showing the points of injection and ignition.

In this figure, the top graph is the raw data and the bottom graph is the derivative. The derivative is determined by using finite differencing and filtering the experimental data using a low-pass digital filter. The derivative is zero except for two key locations: at 0 s there is a spike that corresponds to when the dust is injected, and at 600 s there is another spike which corresponds to when the combustion test begins and the mixture is ignited. The experimental data are in between these two locations. The data before 0 s is also very important because it was used to zero the two signals that make up I/I_0. Now that the experiment portion of the test was isolated, a line was fit to the data to more easily calculate the suspended mass, Figure 20.
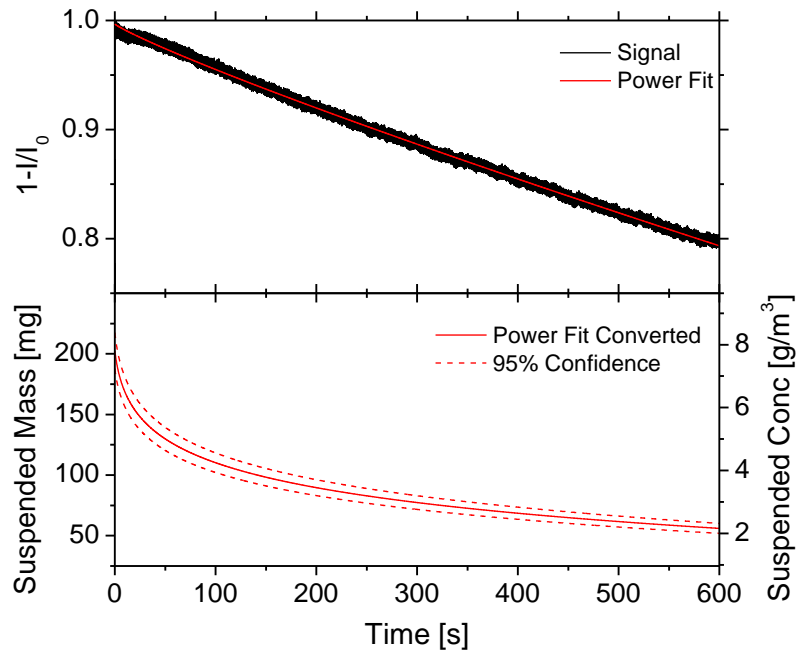
Figure 20. Power fit to the experimental data and the suspended mass evaluated from that fit with 95% confidence intervals.

The suspended mass can be calculated from Eq. (4.5). A few assumptions are important for these calculations. The extinction efficiency is assumed constant, and the data it is based on was measured within the first minute. This assumption is inaccurate because the extinction efficiency factor is based on the particle size distribution, which changes as particles settle out; however, it still provides a suitable estimate. Another important assumption is that the particles of the agglomerates are assumed to be perfect spheres. In reality, they are agglomerates and would have a different extinction efficiency factor and density, as compared to the perfect sphere of equivalent size. The uncertainty in Figure 20 was found using Kline-McClintock uncertainty analysis. Figure 21 gives the breakdown of how each variable contributes to the overall uncertainty.

```
                         ┌──────────────┐
                         │    Mass      │
                         │ Uncertainty  │
                         └──────────────┘
```

d	$\rho_{particle}$	D	Q_{ext}	$Signal$
40 %	35 %	0.5 %	24.5 %	0 %

μ	d		$\Pr(d)$
38 %	33.25 %		

σ	$r_{Al_2O_3}$		μ
2 %	1.75 %		

	ρ_{Al}		σ
	0 %		

	$\rho_{Al_2O_3}$
	0 %
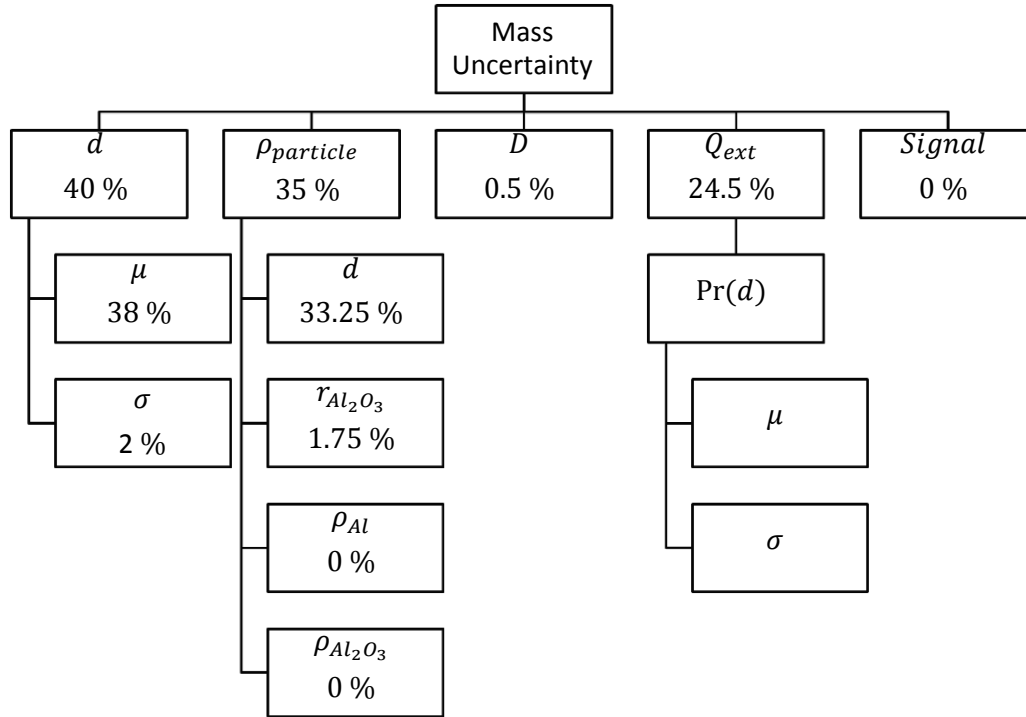
Figure 21. Each variable's contribution to the final suspended-mass uncertainty.

Overall, the largest contributor to the uncertainty is the size distribution because it shows up in two locations. The particle size is used to calculate the mass of each particle, to multiply the number densities by, and also the distribution effects Q_{ext}. The next significant contributor is the uncertainty associated with the volume-averaged particle density. The final uncertainty in the measured amount of suspended mass is shown to be reasonable, ~8%.

4.4 Aerosol Flame Speed

For the present experiments, the nano-aluminum was introduced into a fuel-oxidizer-diluent mixture. In this way, the system under study was therefore one where the flame is initiated in the main fuel-air mixture that contains a seeding of nano-aluminum particles. Two mixtures were used: a stoichiometric $CH_4/O_2/N_2$ mixture with air and one that was oxygen rich, 70% N_2/30% O_2. The reason for the choice of CH_4 is because it is a common and very well-studied fuel, allowing for any results to be attributed to the introduction of the nano-aluminum rather than uncertainties in the fuel's flame speed. The reason for the oxygen-rich air is because in the work by Vissotski [3] it was suspected that the aluminum would not contribute to the reaction if the adiabatic flame temperature was below about 2300 K (i.e., the melting temperature of aluminum oxide).

A typical experiment used the previously discussed dust injection method with the extinction diagnostic set up at all times. This setup allows for a direct measurement of suspended mass from the moment the quarter-turn valve is opened until the moment of ignition. It is easy to see what the suspended mass is at the time of ignition because the laser signal is interrupted by the bright emission of light from combustion and creates a discontinuity in the I_0 signal.

To ensure that the environment inside the vessel is quiescent, the particles are allowed to settle for a minimum of 30 seconds. This minimum wait time comes from the turbulent experiment that was performed in authors' laboratory in the same vessel and from the study by Hwang and Eaton [25] using a similar-sized vessel. It is possible to

push the limits of the minimum wait time because any turbulence would show up in the schlieren images of the flame growth. To analyze the experiments, it was assumed that, since there was a very small amount of aluminum, the burned and unburned gas densities matched those of the neat mixtures.

5. RESULTS AND DISCUSSION

5.1   Extinction Characterization Results

One of the primary objectives of this study was to refine a repeatable method of introducing suspended dust particles into the existing flame speed vessel in the authors' laboratory. One method of evaluating how repeatable the experiments are is to do several "dry" runs, where the gas mixture is either nitrogen or air and no combustion takes place. Such a characterization also allows the researchers to set a target suspended mass, figure out how long the wait time should be, and determine how much mass loading is needed to reach the target. This is particularly useful when performing combustion tests. To this end, several different mass loadings were performed with repeats, and the net results are shown in Figure 22.
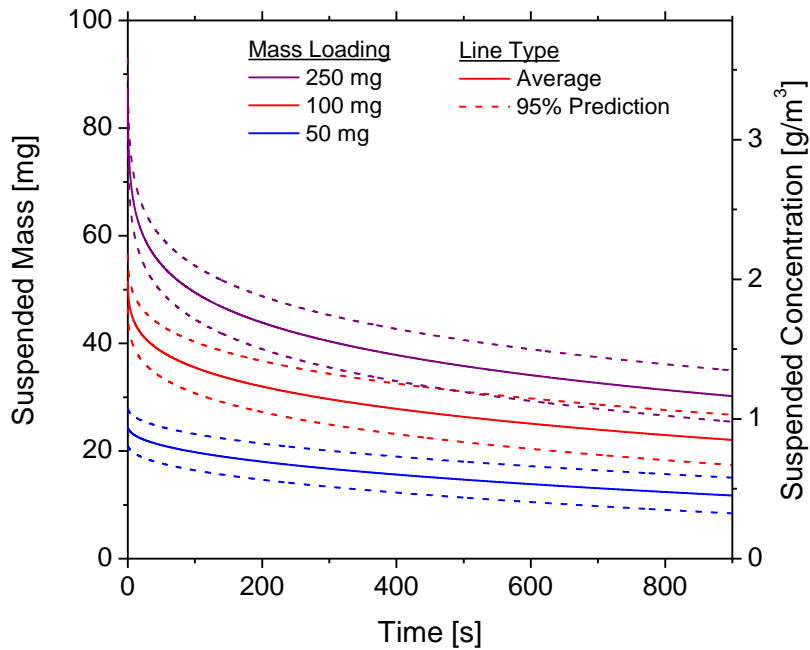
Figure 22. Experimental results of several extinction tests for a range of aluminum dust (initial) loadings.

Figure 22 gives the average for each mass loading and the 95% prediction interval for each mass loading based on both the uncertainty of each experiment and the four experiments that make up each set of mass loading results. Comparing the mass loadings and how much suspended mass was measured, it appears that lower mass loadings were more efficient at carrying the particles into the vessel. At the smaller loading, nearly 50% of the loaded mass was transferred to the vessel; whereas, at the highest loading only about 35% of the loaded mass was transferred. It is suspected that some of the mass was lost to sticking to the tube and vessel walls, in addition to the settling of the larger, agglomerated particles after injection into the vessel.

Spatial uniformity was checked by repeating some test conditions with the laser at two different locations. Results of these repeated tests fell within error of the original tests performed in Figure 22. It was therefore concluded that the system was spatially uniform. This conclusion is strengthened by the repeatability of the DMA/CPC experiments discussed in Section 4.2.

5.2   *Flame Speed Results*

Using Figure 22 as a guide, the first set of combustion experiments was performed. When these experiments failed to show conclusive results, a very high mass loading was performed, 500 mg, and it was ignited as quickly as possible. The extinction results from these initial points are shown in Figure 23 and are representative of the remaining experiments performed with $Al/CH_4/70:30$ $N_2:O_2$.
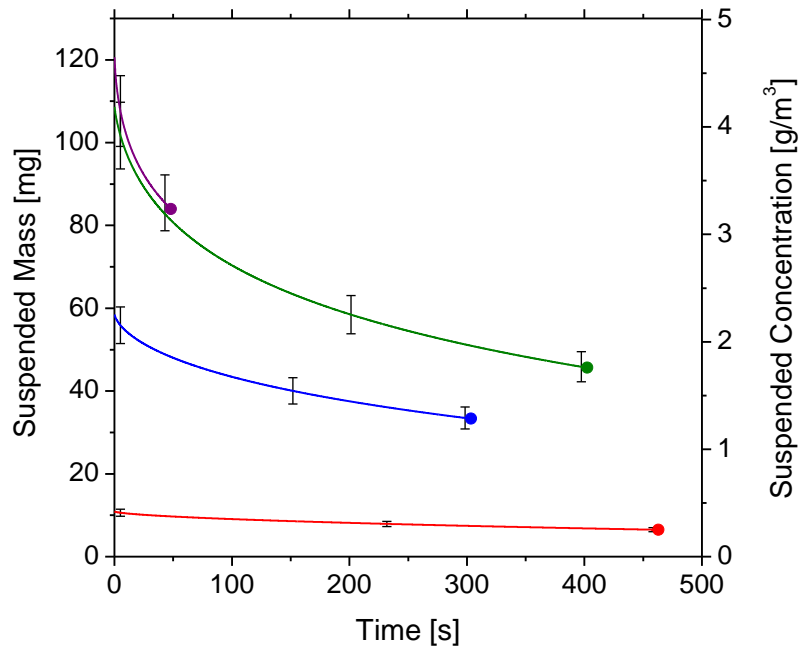
Figure 23. Representative results of extinction during Al/CH$_4$/70:30 N$_2$:O$_2$ experiments. The end point on each curve corresponds to the time at which the mixture was ignited.

Each experiment decays in an exponential fashion. The larger loadings decay much faster but seem to level off at higher suspended masses than those of the smaller loadings. This trend is expected since the larger particles will fall out much quicker and an increased mass loading would have an increased number of smaller particles to stay suspended. It should be noted that the earliest an experiment was performed was at roughly 45 seconds after introduction of the powder. The combustion results are shown in Figure 24, in terms of the laminar flame speed for the corresponding cases in 70:30 N$_2$:O$_2$.
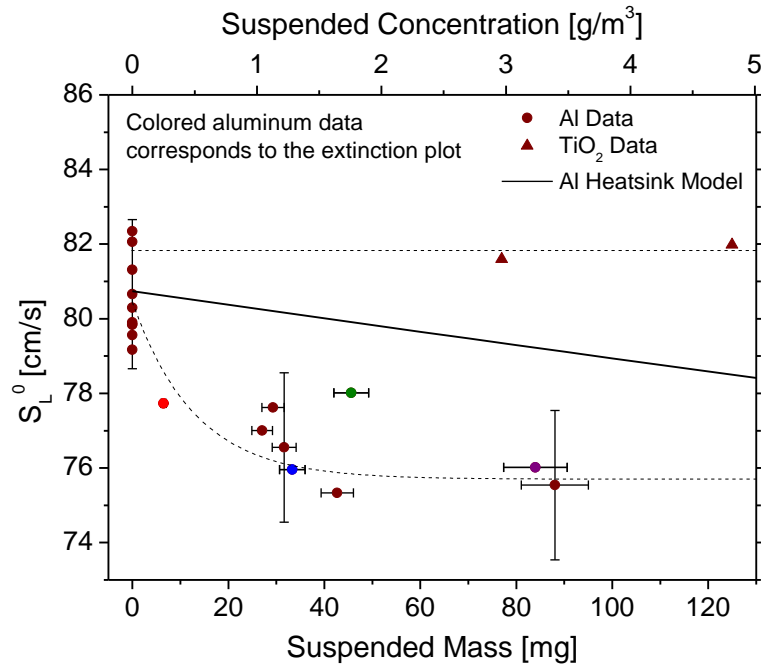
Figure 24. Laminar flame speed results of Al/CH$_4$/70:30 N$_2$:O$_2$ experiments. Dashed lines are only for visual clarity.

In this plot of unburned-unstretched laminar flame speed as a function of suspended mass, there is a noticeable drop in flame speed of about 5 cm/s (when compared to the baseline case with zero suspended mass), which is above the estimated experimental uncertainty, in most cases, of ±2 cm/s. The uncertainty is based on previous methane/air experiments scaled to account for the higher flame speed plus some additional uncertainty to account for non-uniform particles or other issues with the extinction diagnostic. In some cases the decrease in flame speed is within the uncertainty of the neat mixture, but there is a steady decrease in flame speed as the suspended mass increases up to about 60 mg, then the trend seems to flatten out with higher mass loadings.

An interesting note is that two additional experiments were performed with titania, TiO_2, to determine if they too would decrease flame speed, by the results of those tests match very well with the neat mixture. There are no x-error bars on the TiO_2 because it was assumed that they had the same characteristics as the aluminum. Initial mass loadings similar to the higher end of aluminum were used. The goal here was not to accurately measure the suspended mass of TiO_2 but to quickly and qualitatively compare the effects it might have on flame speed with the aluminum.

Similarly for the CH_4/air experiments, extinction measurements were performed in tandem with the combustion experiments over a range of mass loadings. The results of these extinction results, Figure 25, are very similar to those of the CH_4/70:30 N_2:O_2.
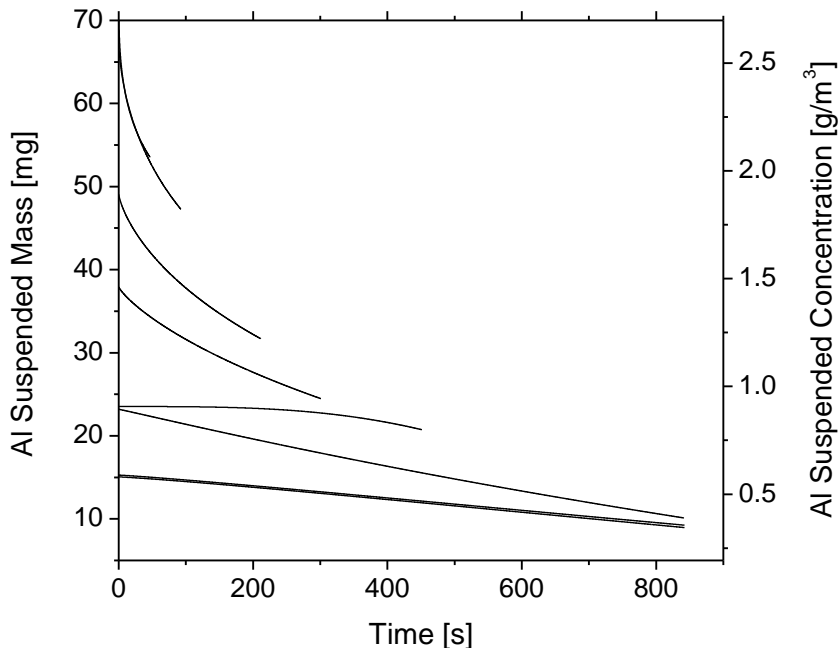
Figure 25. Results of extinction time history measurements during CH_4/air combustion experiments. The curves end at the time of ignition in each case.

45

As with all previous extinction results, there is an exponential decay, and the flame speed results of these experiments resemble those of the CH_4/70:30 N_2:O_2 results. These can be seen in Figure 26.
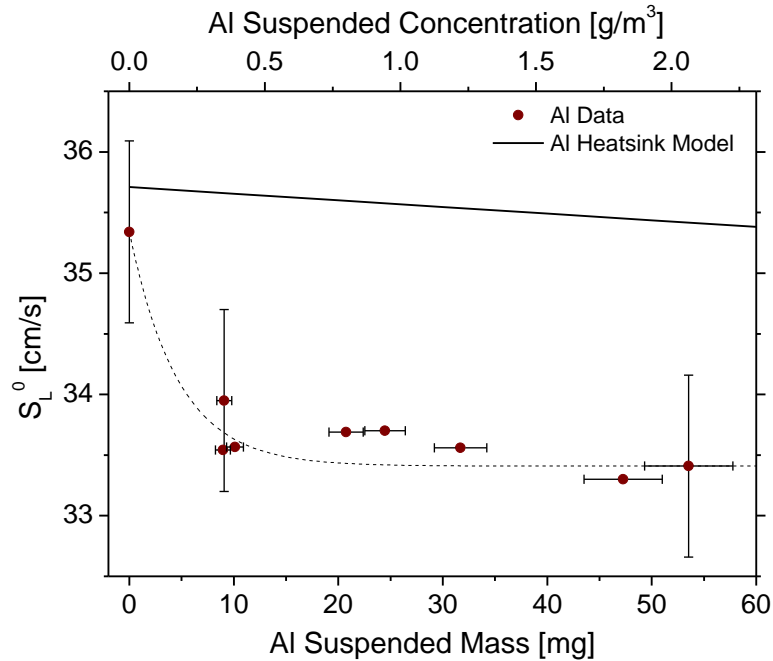
Figure 26. Laminar flame speed results of CH_4/air aerosol experiments. Dashed line is for visual clarity only.

The decrease in flame speed is nearly identical in proportion to the neat mixture for both the air experiments and for the 70:30 N_2:O_2 experiments. This trend lends to the conclusion that the aluminum is having a measureable effect on the laminar flame speed, and in general it decreases it. It is suspected that part of the cause for this decrease in flame speed is because some energy from the heat of combustion is used to heat up the aluminum particles. The aluminum particles can only react if they are heated enough to

either diffuse through the oxide layer or crack it so that the aluminum is exposed. Based on the theoretical calculations provided previously, the loss of energy is not sufficient to decrease the flame speed to this level. For example, the particle heating should account for about half or less of the total decrease in flame speed seen in Figures 24 and 26. It is therefore suspected that the aluminum particles are having an additional kinetic or diffusive effect to decrease the flame speed by this much.

A decrease in flame speed matches the recent experiments performed at McGill University with both iron and aluminum particles in a similar hybrid methane mixture but using a Bunsen burner setup [26, 27]. The magnitude of the decrease in the tests in this thesis differs from their experiments in that they did not have as much of a decrease per concentration; however, the experiments cannot be directly compared as the McGill particles are several times larger. Because of the size difference, it is expected that their particles would not have the same contribution to the reaction process as the nano-sized particles in this thesis. In their study, it was found that at some point this decrease in flame speed will plateau and the flame will be a pure aluminum flame.

5.3 Additional Experiments

An interesting phenomenon that can be visually observed is that the nano-particles seemed to accelerate the onset of instability in the flames. A comparison of five experiment's raw images is shown in Figure 27. The intrusion in the bottom of all experiments is the optical setup from the laser extinction diagnostic.
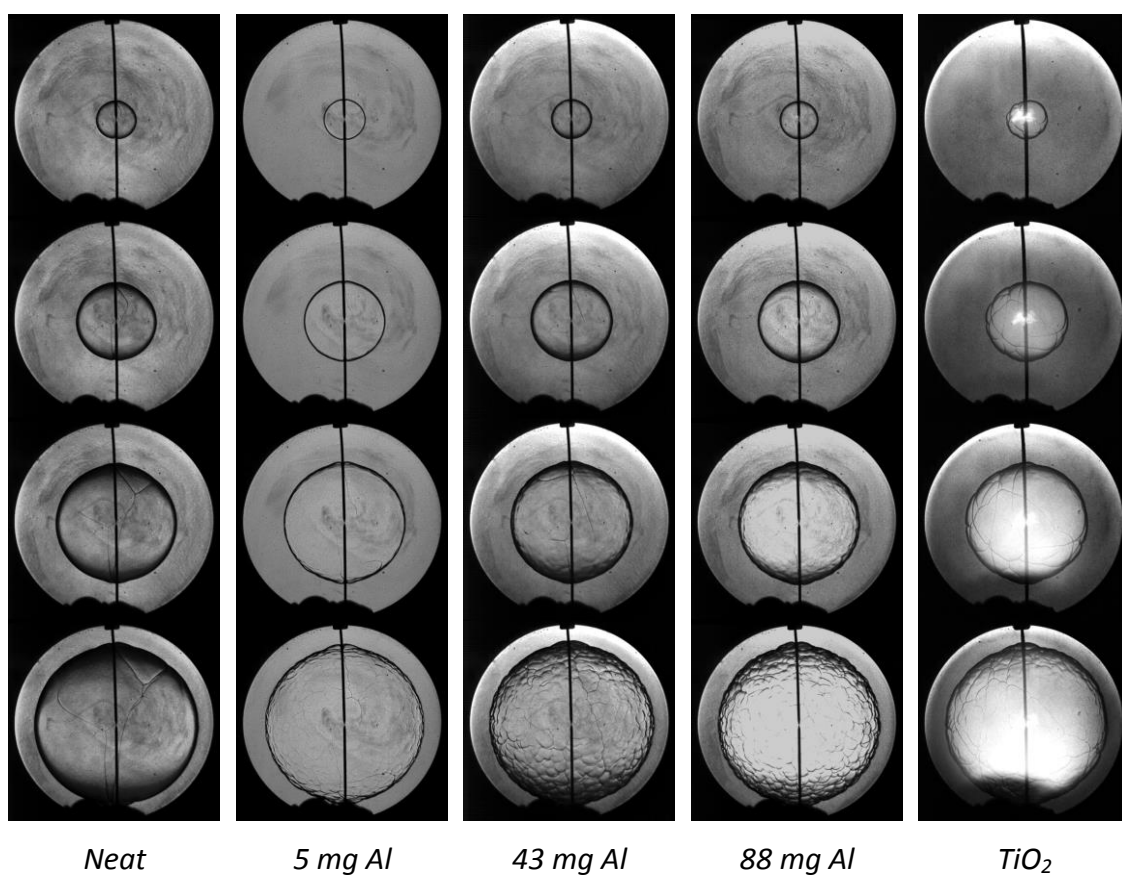

| Neat | 5 mg Al | 43 mg Al | 88 mg Al | TiO_2 |

Figure 27. Image sequences of neat $CH_4/70{:}30$ $N_2{:}O_2$ flames and aluminum/titania hybrid flames compared at equivalent radii.

In comparing the neat case from Figure 27 to all other cases, it is evident that the onset of instability is occurring sooner; time increases as the flames grow. The neat case does not even start to become turbulent by the end of the experiment whereas the other four cases all start to become turbulent around the second or third frame of their time series. This phenomenon is further demonstrated by looking at the final frame of three experiments in Figure 28.

Neat   *43 mg Al*   *TiO$_2$*
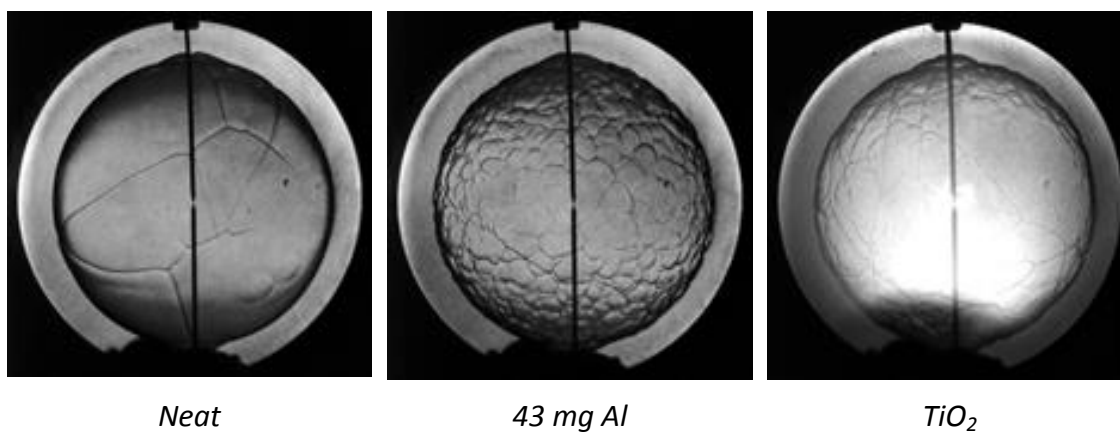
Figure 28. Final raw images of a neat CH$_4$/70:30 N$_2$:O$_2$ flame and aluminum/titania hybrid flames.

The difference between the aluminum and titania hybrid mixtures to the neat methane mixture is a stark contrast because instabilities are prominent in the hybrid mixtures. This observation means that somehow the nano-particles themselves are causing an effect on the combustion process. Of the two tests performed with titania, the flame speed remained the same as the neat methane flame (as mentioned above) despite the flame structure looking somewhat similar to the aluminum/methane hybrid flame,

which further reinforces that the nano-particles themselves are causing the flame surface instability.

In an attempt to determine if aluminum was combusting within the reaction zone, a spectrometer was used to capture the combustion event. The results of these tests can be seen along with the identified species in Figure 29 [26, 28-30].
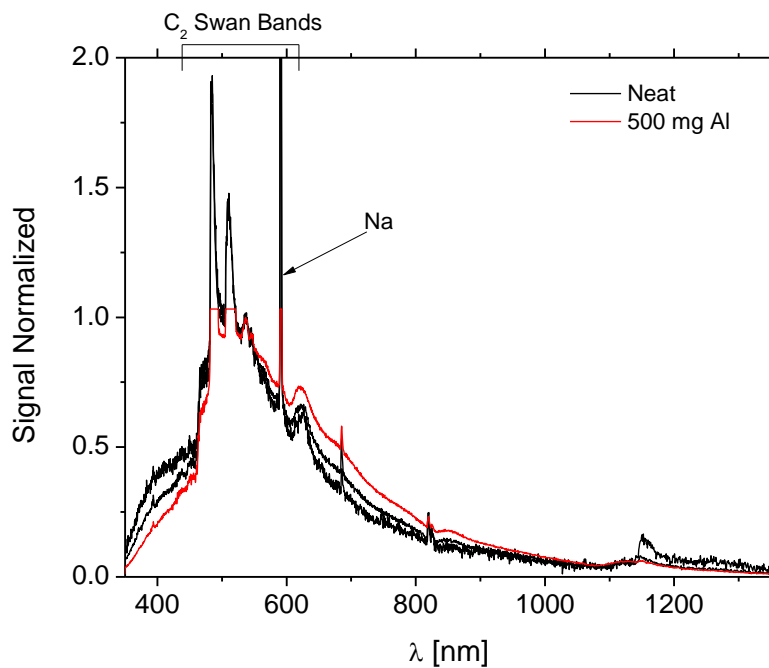
Figure 29. Spectra during $Al/CH_4/70:30\ N_2:O_2$ combustion experiments normalized by 536.7 nm.

At first glance, in comparing the neat experiments to the aluminum experiment, it appears that there are small differences between the experiments, but this is because the blackbody radiation is different for each test. The spectrometer used during these tests was limited in that it could not be set to automatically trigger and its integration time had

a minimum of 3 ms. These limitations mean that the spectra integrate over a third of the flame residence time and that it is not expected that they line up temporally. Taking into account how the limitations affect the experiment, it makes sense that the spectra would have different blackbody radiation profiles because they are at different times in the life of the flame and therefore different temperatures. Looking closer at the spectra peaks, there appears to be no difference in any of the experiments. However, these spectra tests are inconclusive at this time and do not necessary rule out the possibility of aluminum combustion, but it is possible that there is none since no expected features of aluminum oxidation such as AlO emission were seen in the recorded spectra. Further study is required using time-resolved emission spectra.

6. CONCLUSIONS AND FUTURE WORK

A method of introducing dust into an existing spherical flame speed vessel was successfully refined by increasing the repeatability and ease at which experiments could be performed. Nano-aluminum was characterized for these experiments using a combination of DMA/CPC. It was found that the average particle/agglomerate size was about 450 nm, and the most probable particle/agglomerate size was about 300 nm. Using the size distribution, a theoretical extinction efficiency factor was calculated using Mie scattering. This extinction factor allowed for accurate measurement of suspended aluminum prior to a live flame speed experiment with a small uncertainty of 8%.

Combustion tests were analyzed with optical techniques that allow for visual inspection to determine the onset of flame instability as well as tracking the flame edge as a function of time to determine laminar flame speed. The resulting flame speed results show that adding nano-aluminum does influence combustion by decreasing the flame speed. A theoretical calculation was performed under the assumption that changes in the kinetic or diffusive effects were negligible and that the aluminum was acting solely as a heat sink. The resulting predictions showed a decrease in flame speed but not as much as the experimentally determined decrease nor did the calculations follow the same trend. This discrepancy leads to the conclusion that there might be some diffusive or kinetic effect from the presence of the aluminum. An interesting discovery was that when nano-aluminum was added, the flames started to show instabilities forming by the end of the experiment.

To verify that decrease in flame speed was due to aluminum, and not because of the presence of particles, two tests were performed with nano-titania. Since titania should not react, the comparison between the two different particle types should give an indication of what was caused by the presence of nano-particles and what was unique to aluminum. It was found that the accelerated instabilities are caused by nano-particles in general, not specifically just the nano-aluminum particles. It was also found that the nano-titania did not decrease the flame speed, indicating that a phenomenon linked to nano-aluminum was causing the decrease in flame speed. Additional conservation of energy calculations to determine how much titania decreases the flame speed, if acting as a heat sink, need to be performed.

In the future, several issues need to be addressed. To expand this study, and all future heterogeneous studies, a larger amount of powder mass needs to be injected into the system. This larger level would allow for better comparison with conventional literature data (using fast-injection, spherical explosion vessels) as well as giving the possibility of not using a hybrid mixture but rather a pure dust/oxidizer mixture. An aluminum flame gives off much more light than a methane flame. To prevent this extra light from burning out the CCD of the camera, some kind of neutral density filter will be needed. Combining the decreased light to save the CCD with the increased light extinction associated with more mass will cause a problem with the schlieren optics and visibility of the viewing port window. The analysis procedure currently requires that the viewing port be visible so that a correlation can be drawn between the frame size in

53

pixels to the physical dimensions of the vessel. Without this relationship between pixels and length in cm, the images will not be able to be related to a physical quantity.

For more experiments to be performed, it would be prudent to have a better method of cleaning out the vessel. Currently, the vessel endcap must be removed, which is roughly 50 lbs., while wearing safety equipment. The inside of the vessel is covered in aluminum nano-particles and must be carefully cleaned with acetone and towels. The piping is unable to be cleaned, only flushed with higher-than-normal pressure. A better method of cleaning the vessel might improve repeatability as well as be safer for those cleaning it. One idea to solve this issue would be to include a water flushing system. This process would clump particles so that even if the endcap needed to be removed there would be less risk of exposure to nanoscale dust, and simultaneously it would remove more particles from both the tubing and the test vessel.

Because these are very small particles they get everywhere. The pressure must be carefully managed so that there is never a pressure gradient towards the manifold while the dust is loaded. Additionally, the small particles cause leaks in all of the valves that are exposed to them, including the pneumatic valves. Removing these concerns would make the experiment less prone to contamination.

It goes without saying that experiments could be performed in which the parent gas mixture could be altered, the dust material could be changed, or dust size could be varied, but another interesting series of tests would be to use either laser spectroscopy or a spectrometer to measure the evolution of certain species within the flame. This would

provide better data for comparison to a chemical kinetics mechanism. Having such a system would also give the ability to detect if the dust present is reacting.

REFERENCES

[1]   A. Dahoe; T. van Velzen; L. Sluijs; F. Neervoort; S. Leschonski; S. Lemkowitz; P. van der Wel; B. Scarlett in: *Construction and operation of a 20-litre dust explosion sphere at and above atmospheric conditions*, Loss Prevention and Safety Promotion in the Process Industries, Proceedings of the 8th International Symposium, 1995; pp 285-302.

[2]   K.L. Cashdollar, J. Loss Prevent. Proc. 13 (3-5) (2000) 183-199.

[3]   A.J. Vissotski. Development of an Experimental Facility for Flame Speed Measurements in Powdered Aerosols. M.S., Texas A&M University, 2012.

[4]   D. Kalitan; E. Petersen in: *Nano-aluminum aerosol characterization with application to heterogeneous shock-tube combustion*, 5th US Combustion Meeting, 2007.

[5]   S. Ravi; T.G. Sikes; A. Morones; C.L. Keesee; E.L. Petersen, *Comparative study on the laminar flame speed enhancement of methane with ethane and ethylene addition*, Proc. Combust. Inst. (2014), doi:10.1016/j.proci.2014.05.130 (In Press).

[6]   F.P. Incropera, Fundamentals of Heat and Mass Transfer, Wiley, Hoboken, New Jersey, 2007.

[7]   E.E.S. Michaelides, Heat and Mass Transfer in Particulate Suspensions, Springer, New York, 2013.

[8]   X.-Q. Wang; A.S. Mujumdar, Int. J. Therm. Sci. 46 (1) (2007) 1-19.

[9]   M. Hu; G.V. Hartland, J. Phys. Chem. B 106 (28) (2002) 7029-7033.

[10]   E.L. Petersen; S.D. Smith, AIAA Paper 973 (2004) 5-8.

[11]   P.D. Desai, Int. J. Thermophys. 8 (5) (1987) 621-638.

[12]   P.H. Zhang; R.Z. Chang; Z. Wei; H. Cao; X.N. Zhou, Int. J. Thermophys. 7 (4) (1986) 811-819.

[13]   NIST Chemistry WebBook, NIST Standard Reference Database Number 69. http://webbook.nist.gov (June 2014).

[14]   W.K. Metcalfe; S.M. Burke; S.S. Ahmed; H.J. Curran, Int. J. Chem. Kinet. 45 (10) (2013) 638-675.

[15]   N. Ikemiya; J. Umemoto; S. Hara; K. Ogino, ISIJ Int. 33 (1) (1993) 156-165.

[16]   M.J. Assael; K. Kakosimos; R.M. Banish; J. Brillo; I. Egry; R. Brooks; P.N. Quested; K.C. Mills; A. Nagashima; Y. Sato; W.A. Wakeham, J. Phys. Chem. Ref. Data 35 (1) (2006) 285-300.

[17]   J. De Vries. A study on spherical expanding flame speeds of methane, ethane, and methane/ethane mixtures at elevated pressures. Ph.D., Texas A&M University, 2009.

[18]   W. Lowry; J. de Vries; M. Krejci; E. Petersen; Z. Serinyel; W. Metcalfe; H. Curran; G. Bourque, J. Eng. Gas. Turb. Power. 133 (9) (2011) 091501-091501.

[19]   D. Reid. Synthesis, Properties, and Performance of Polymer-Matrix Nanocomposites for Energetic Applications. Ph.D., University of Central Florida, 2012.

[20]   D. Swinehart, J. Chem. Educ. 39 (7) (1962) 333.

[21]   C.F. Bohren; D.R. Huffman, Absorption and Scattering of Light by Small Particles, Wiley-Interscience, New York, 1983.

[22]   O. Peña-Rodríguez; P.P. González Pérez; U. Pal, Int. J. Spectrosc. 2011 (2011) 583743, 1-10.

[23]   D.R. Huffman, Extinction Measurements on Aluminum and Carbon Smoke Particles from Far Infrared to Far Ultraviolet in: DTIC Document-ADA179003, 1987.

[24]   A.D. Rakić, Appl. Opt. 34 (22) (1995) 4755-4767.

[25]   W. Hwang; J.K. Eaton, Exp. Fluids 36 (3) (2004) 444-454.

[26]   M. Soo; P. Julien; S. Goroshin; J.M. Bergthorson; D.L. Frost, Proc. Combust. Inst. 34 (2) (2013) 2213-2220.

[27]   P. Julien; S. Whiteley; S. Goroshin; M.J. Soo; D.L. Frost; J.M. Bergthorson, *Flame structure and particle-combustion regimes in premixed methane–iron–air suspensions*, Proc. Combust. Inst. (2014), doi:10.1016/j.proci.2014.05.003 (In Press).

[28]   J.M. Peuker; P. Lynch; H. Krier; N. Glumac, Propellants, Explos., Pyrotech. 38 (4) (2013) 577-585.

[29]   T.S. Cheng; C.Y. Wu; Y.H. Li; Y.C. Chao, Combust. Sci. Technol. 178 (10-11) (2006) 1821-1841.

[30]   M.M. Tripathi; S.R. Krishnan; K.K. Srinivasan; F.-Y. Yueh; J.P. Singh, Fuel 93 (2012) 684-691.